

Magnetic field spreading from stellar and galactic dynamos into the exterior

AXEL BRANDENBURG,^{1,2,3,4} OINDRILA GHOSH,⁵ FRANCO VAZZA,^{6,7} AND ANDRII NERONOV^{8,9}

¹*Nordita, KTH Royal Institute of Technology and Stockholm University, Hannes Alfvéns väg 12, SE-10691 Stockholm, Sweden*

²*The Oskar Klein Centre, Department of Astronomy, Stockholm University, AlbaNova, SE-10691 Stockholm, Sweden*

³*McWilliams Center for Cosmology & Department of Physics, Carnegie Mellon University, Pittsburgh, PA 15213, USA*

⁴*School of Natural Sciences and Medicine, Ilia State University, 3-5 Cholokashvili Avenue, 0194 Tbilisi, Georgia*

⁵*Oskar Klein Centre for Cosmoparticle Physics, Department of Physics, Stockholm University, AlbaNova, 10691 Stockholm, Sweden*

⁶*Dipartimento di Fisica e Astronomia, Università di Bologna, Via Gobetti 93/2, 40129 Bologna, Italy*

⁷*INAF Istituto di Radioastronomia, Via P. Gobetti 101, 40129 Bologna, Italy*

⁸*Université Paris Cité, CNRS, Astroparticule et Cosmologie, 75006 Paris, France*

⁹*Laboratory of Astrophysics, École Polytechnique Fédérale de Lausanne, 1015 Lausanne, Switzerland*

ABSTRACT

The exteriors of stellar and galactic dynamos are usually modeled as a current-free potential field. A more realistic description might be that of a force-free magnetic field. Here, we suggest that, in the absence of outflows, neither of those reflect the actual behavior when the magnetic field spreads diffusively into a more poorly conducting turbulent exterior outside dynamo. In particular, we explain why the usual ordering of the dipole magnetic field being the most slowly decaying one is altered, and that the quadrupole can develop a toroidal component that decays even more slowly with radial distance. This is a robust feature that persists even for spatially nonuniform magnetic diffusivities. It is best seen for spherical dynamo volumes and becomes more complicated for oblate ones. In either case, however, those fields are confined within a magnetosphere beyond which the field drops exponentially. We demonstrate that the Faraday displacement current, which plays a role in a vacuum, can safely be neglected in all cases. The superposition of magnetic fields from galaxies in the outskirts of the voids between galaxy clusters can therefore not explain the void magnetization of the intergalactic medium, reinforcing the conventional expectation that those fields are of primordial origin. For quadrupolar configurations, the synchrotron emission from the magnetosphere is found to be constant along concentric rings. The dipolar and quadrupolar configurations display large-scale radial trends that are potentially distinguishable with existing radio telescopes.

Keywords: Magnetic fields (994); Hydrodynamics (1963)

1. INTRODUCTION

The magnetic fields in stars and galaxies can be explained by dynamo action converting the kinetic energy in the turbulence and the differential rotation into magnetic energy. Such systems are traditionally computed by assuming that the magnetic field outside the dynamo domain continues as a current-free potential field. Mathematically, this can be formulated as a suitable boundary condition applied on the outer radius of a spherical (Steenbeck & Krause 1969) or an ellipsoidal domain (Stix 1975). In cylindrical and several other coordinate systems, on the other hand, there exists no method to apply a potential field boundary condition. One possibility is then to adopt a perfectly conducting boundary condition (Meinel et al. 1990). How-

ever, a more physical procedure might be to embed the galaxy in a poorly conducting exterior (Eltner et al. 1990; Brandenburg et al. 1990), because this would approximate a vacuum in the limit of zero conductivity.

The assumption of a vacuum outside the dynamo was never thought to be more than just a mathematically convenient construct. However, in recent work of Garg et al. (2025), a vacuum was assumed to exist even in the far-field of galaxies. Their study, which does not involve outflows or winds of any type, spawned subsequent investigations that addressed the question what the nature of the magnetic field in the far-field of galaxies actually is (Seller & Sigl 2025; Ghosh et al. 2026). The present paper is a follow-up of our earlier work (Ghosh et al. 2026). Here, we focus on a more de-

tailed numerical study, approach in some cases the limit of extremely poor conductivity, and make contact with possible measurements of synchrotron emission.

It is commonly assumed that a more realistic boundary condition of a dynamo corresponds to an electrically conducting exterior, although not necessarily to a perfectly conducting one. In addition, if the density of the exterior is low and the exterior is at rest, the magnetic field would be force-free, i.e., the cross product of current density and magnetic field vanishes. Also in the context of plasma confinement configurations, force-free magnetic fields tend to be more realistic than the assumption of a vacuum (Freidberg 2014). Since in MHD, the current density is proportional to the curl of the magnetic field, both fields must then be parallel to each other. Such fields would therefore be eigenfunctions of the curl operator and are also known as Chandrasekhar-Kendall functions (after the early paper by Chandrasekhar & Kendall 1957).

Adopting a perfectly force-free magnetic field is generally problematic because it might topologically not be realizable and it would also take significant time to establish such a field in the vast exterior of a dynamo. Therefore, to alleviate this problem, a commonly used approach in solar physics is the magneto-frictional one (Yang et al. 1986). Here, the Lorentz force is allowed to drive flows through a friction term. These flows tend to relax the field until the force is minimized. In a similar approach, we study here the spreading of galactic magnetic fields into intergalactic space by solving the mean-field momentum equation and modeling the dynamo exterior as a medium with a certain viscosity and electric conductivity. A vacuum would correspond to the limit of very small conductivity or very large magnetic diffusivity. A large effective magnetic diffusivity emerges in a turbulent environment when modelling the large-scale field as an average or mean field, $\overline{\mathbf{B}}$, where the overbar denotes some suitable averaging. However, as we explain below, the diffusivity needed to reproduce the electric properties of a vacuum would be at least eight orders of magnitude larger than what can reasonably be explained by turbulence.

It is useful to represent the resulting magnetic field as a multipole expansion with terms proportional to spherical harmonics $Y_\ell^m(\theta, \phi)$, where ℓ and m are the spherical harmonic degree and order, respectively. For a vacuum, the magnetic field decays with radius r like $r^{-(\ell+2)}$. The lowest multiple is the dipole with $\ell = 1$, so the field decays like r^{-3} , while for a quadrupole, $\ell = 2$, so the field decays like r^{-4} . In an electrically conducting environment, magnetic fields are expected to be close to force-free and can then decay differently. If the gas pressure

is negligible, force-free magnetic fields obey $\overline{\mathbf{J}} \times \overline{\mathbf{B}} = 0$, i.e., the current density $\overline{\mathbf{J}} = \nabla \times \overline{\mathbf{B}}/\mu_0$ with μ_0 being the vacuum permeability, is parallel to $\overline{\mathbf{B}}$. This means that $\nabla \times \overline{\mathbf{B}} = \alpha_{\text{ff}} \overline{\mathbf{B}}$, where α_{ff} is a coefficient that must be constant along the magnetic field line, but it can vary perpendicular to it (Priest 1982).

To explain the toroidal magnetic fields observed around solar-type stars, Bonanno (2016) and Bonanno & Del Sordo (2017) considered force-free magnetic fields in mean-field dynamo exteriors. They assumed the coronal magnetic field of those stars to be harmonic, but they did not consider the question how such magnetic field configurations can be achieved in a finite time. Here, we show that such fields can only be produced within a finite but slowly expanding magnetosphere around the dynamo. This also has applications to galactic dynamos and the question whether such configurations can explain the magnetic field in the voids between galaxy clusters (Garg et al. 2025; Seller & Sigl 2025; Ghosh et al. 2026).

Ghosh et al. (2026) showed that the growth of the magnetosphere changes from ballistic to diffusive once the dynamo saturates. They also demonstrated that a quadrupolar magnetic field in the magnetosphere decays with radius r only like r^{-2} , which is slower than the r^{-3} decay of a dipolar field—both in a vacuum and in a conducting exterior. Here we present a detailed analysis of these empirical findings. We also elucidate the reason for the slow radial decay for quadrupolar fields. In particular, we explore the limit toward the vacuum case considered by Garg et al. (2025). We also compute the resulting synchrotron emission from the slow radially decaying quadrupolar field.

In Section 2, we present the details of our model, allowing for different profiles of the effective magnetic diffusivity, as well as feedback from mean flows and/or a finite speed of light in some cases. Our results about the establishment of a time-dependent magnetosphere are discussed in Section 3. In Section 4, we discuss new observational constraints in terms of synchrotron radio emission, which go beyond the rotation measure diagnostics presented in Ghosh et al. (2026). Finally, we conclude in Section 5.

2. OUR MODEL

2.1. Basic equations

We solve the mean-field dynamo equations using spherical coordinates, (r, θ, ϕ) . Before making the MHD approximation, in which the Faraday displacement current is omitted, we begin with the full Maxwell equations that are also applicable to an extremely poorly conducting medium or the vacuum considered by Garg et al.

(2025). To quantify the difference between a poorly conducting exterior and a vacuum, we also include in some cases the Faraday displacement current. The detailed motivation for such a study along with first results was already presented by Ghosh et al. (2026).

The displacement current can play a role when the ordinary current density is small. We assume that the mean current density $\overline{\mathbf{J}}$ obeys Ohm's law, which, in our case, takes the form

$$\overline{\mathbf{J}} = \sigma(\overline{\mathbf{E}} + \overline{\mathbf{U}} \times \overline{\mathbf{B}} + \overline{\mathbf{u}} \times \overline{\mathbf{b}}), \quad (1)$$

where σ is the microphysical conductivity, $\overline{\mathbf{E}}$ is the mean electric field, $\overline{\mathbf{U}}$ is the mean velocity, $\overline{\mathbf{B}}$ is the mean magnetic field, and $\overline{\mathbf{u}} \times \overline{\mathbf{b}}$ is the mean electromotive force resulting from the small-scale velocity and magnetic fields, \mathbf{u} and \mathbf{b} , respectively. In its simplest form, the mean electromotive force can be written as

$$\overline{\mathbf{u}} \times \overline{\mathbf{b}} = \alpha \overline{\mathbf{B}} - \eta_{\text{turb}} \mu_0 \overline{\mathbf{J}}, \quad (2)$$

where α is a coefficient that emerges in the calculation of $\overline{\mathbf{u}} \times \overline{\mathbf{b}}$ for helical turbulence (Moffatt 1978). It can lead to the growth and sustenance of a mean magnetic field and is generally referred to as the α effect. Furthermore η_{turb} is the turbulent magnetic diffusivity.

It is convenient to define the microphysical magnetic diffusivity $\eta = (\mu_0 \sigma)^{-1}$ along with the total (effective) magnetic diffusivity $\eta_{\text{eff}} = \eta + \eta_{\text{turb}}$. Ohm's law for the mean current density can then be written as

$$\mu_0 \overline{\mathbf{J}} = (\overline{\mathbf{E}} + \overline{\mathbf{U}} \times \overline{\mathbf{B}} + \alpha \overline{\mathbf{B}}) / \eta_{\text{eff}}. \quad (3)$$

The term $\mu_0 \overline{\mathbf{J}}$ enters as the second one on the right-hand side of the averaged Ampere–Maxwell equation,

$$\frac{1}{c^2} \frac{\partial \overline{\mathbf{E}}}{\partial t} = \nabla \times \overline{\mathbf{B}} - \mu_0 \overline{\mathbf{J}}, \quad (4)$$

where c is the speed of light.

The full set of Maxwell equations can then be written as

$$\frac{\partial \overline{\mathbf{A}}}{\partial t} = -\overline{\mathbf{E}}, \quad \overline{\mathbf{B}} = \nabla \times \overline{\mathbf{A}}, \quad (5)$$

along with

$$-\left(1 + \frac{\eta_{\text{eff}}}{c^2} \frac{\partial}{\partial t}\right) \overline{\mathbf{E}} = \overline{\mathbf{U}} \times \overline{\mathbf{B}} + \alpha \overline{\mathbf{B}} - \eta_{\text{eff}} \nabla \times \overline{\mathbf{B}}, \quad (6)$$

where $\overline{\mathbf{A}}$ is the mean magnetic vector potential, so the mean magnetic field is given by $\overline{\mathbf{B}} = \nabla \times \overline{\mathbf{A}}$, which satisfies the constraint $\nabla \cdot \overline{\mathbf{B}} = 0$. The mean charge density is given by $\overline{\rho}_e = \epsilon_0 \nabla \cdot \overline{\mathbf{E}}$, where $\epsilon_0 = 1/\mu_0 c^2$ is the vacuum permittivity. Here, we have adopted the Weyl gauge, i.e., the electrostatic potential vanishes.

The Faraday displacement current, $\epsilon_0 \partial \overline{\mathbf{E}} / \partial t$, can be neglected when $\eta_{\text{eff}} \ll \tau c^2$, where τ is a characteristic time scale. In that limit, the MHD approximation applies and the terms on the rhs of Equation (6) can directly be inserted on the rhs of Equation (5) to yield the familiar induction equation. We refer to Appendix A for a discussion of the dispersion relation of a dynamo with α effect and a finite value of c for the simple Cartesian case in a periodic domain with constant coefficients and no feedback from mean gas motions, i.e., $\overline{\mathbf{U}} = 0$. There, and later in the present paper, we identify τ with the light travel time, i.e., with $(ck)^{-1}$ or R/c , where k is the wavenumber of the lowest dynamo mode in a periodic domain, and R is the radius of the dynamo in an open domain. Thus, we have $\eta_{\text{eff}} \ll c/k$ and $\eta_{\text{eff}} \ll cR$ in these two cases.

It is important to stress that the nature of the basic equations changes from parabolic to hyperbolic when the displacement current is included. This also implies that the computational time step constraint changes from being quadratic to linear in the mesh spacing. This can significantly alleviate the computational restrictions of explicit schemes.

To account for the mean gas motions driven by the magnetic field, we also solve in some cases the momentum equation assuming the gas to be isothermal, so the sound speed c_s is constant and the mean pressure $\overline{p}(x, z, t)$ is given by $\overline{p} = \overline{\rho} c_s^2$. The mean-field hydromagnetic equations have previously been solved by many different authors starting with the work by Schüssler (1979) in Cartesian geometry and Brandenburg et al. (1992), Kitchatinov & Rüdiger (1995), and Rempel (2006). The full system of equations is then to be complemented by those for \overline{p} and $\overline{\mathbf{U}}$, i.e.,

$$\frac{D \ln \overline{p}}{Dt} = -\nabla \cdot \overline{\mathbf{U}}, \quad (7)$$

$$\frac{D \overline{\mathbf{U}}}{Dt} = -c_s^2 \nabla \ln \overline{p} + [\overline{\mathbf{J}} \times \overline{\mathbf{B}} + \nabla \cdot (2\nu_{\text{eff}} \overline{\rho} \overline{\mathbf{S}})] / \overline{\rho}, \quad (8)$$

where $D/Dt = \partial/\partial t + \overline{\mathbf{U}} \cdot \nabla$ is the advective derivative and $\overline{\mathbf{S}}$ is the rate-of-strain tensor of the mean flow with the components $\overline{S}_{ij} = (\overline{U}_{i;j} + \overline{U}_{j;i})/2 - \delta_{ij} \nabla \cdot \overline{\mathbf{U}}/3$. Here, semicolons denote covariant derivatives.

There are three mean-field parameters: the α effect, the turbulent (effective) viscosity ν_{eff} , and the turbulent (effective) magnetic diffusivity η_{eff} . In addition to the macrophysical backreaction from the mean Lorentz force $\overline{\mathbf{J}} \times \overline{\mathbf{B}}$, we also allow for microphysical feedback in the form of α quenching (Ivanova & Ruzmaikin 1977) and assume α to be proportional to a quenching factor

$$Q(\overline{\mathbf{B}}) = 1/(1 + \overline{\mathbf{B}}^2/B_{\text{eq}}^2), \quad (9)$$

where B_{eq} is the equipartition field strength above which α begins to be affected by the feedback from the Lorentz force of the small-scale magnetic field.

2.2. Details of the model

In the following, we adopt the computational domain $r_{\text{in}} \leq r \leq r_{\text{out}}$ and $0 \leq \theta \leq \pi/2$, and assume axisymmetry, i.e., $\partial/\partial\phi = 0$. In Equation (3), we must specify spatial profiles for α and η_{eff} . To model a localized dynamo-active region, we choose α to be finite around the origin and zero outside the dynamo region.

In Equation (3), we must specify spatial profiles for α and η_{eff} . We mostly study spherical dynamo regions with a given radius R , but in some cases, we also allow the region to be oblate. In those cases, the disk thickness in the z direction, i.e., along the axis, is denoted by h . To model a smooth transition, we choose an error function profile. In addition, α should be antisymmetric about $z = 0$. This is accomplished by multiplying with an additional z/h factor. Thus, we write the α effect in the form

$$\alpha = \alpha_0 \frac{z}{h} \frac{Q(\overline{\mathbf{B}})}{2} \left[1 - \operatorname{erf} \frac{\sqrt{(\varpi/R)^2 + (z/h)^2} - 1}{w/R} \right], \quad (10)$$

where α_0 is a constant, $\varpi = r \sin \theta$ is the cylindrical radius, $z = r \cos \theta$ is the height above the midplane, and w is the width of the transition from the dynamo-active region to the exterior. For $h = R$, the dynamo region is spherical.

For η_{eff} , we allow the effective magnetic diffusivity to be a larger value $\eta_{\text{eff}}^{\text{ext}}$ outside the dynamo region and equal to $\eta_{\text{eff}}^{\text{int}} \leq \eta_{\text{eff}}^{\text{ext}}$ within the dynamo region. We construct the profile for η_{eff} similarly to that of α , except that it is symmetric about $z = 0$ and there is no quenching factor. Thus, we choose the profile for η_{eff} to be given by

$$\eta_{\text{eff}} = \eta_{\text{eff}}^{\text{int}} + \frac{\eta_{\text{eff}}^{\text{ext}} - \eta_{\text{eff}}^{\text{int}}}{2} \left[1 + \operatorname{erf} \frac{\sqrt{(\varpi/R)^2 + (z/h)^2} - 1}{w/R} \right]. \quad (11)$$

We also study some models where η_{eff} is uniform throughout the domain, i.e., $\eta_{\text{eff}}^{\text{ext}} = \eta_{\text{eff}}^{\text{int}}$, as well as models where η_{eff} grows gradually in the exterior like a power law. In those cases, we take

$$\eta_{\text{eff}}^{\text{ext}} = \eta_{\text{eff}}^{\text{int}} (1 + r/r_0)^m, \quad (12)$$

where $m > 0$ is the exponent and the parameter r_0 determines how rapidly η_{eff} grows in the exterior.

To avoid the coordinate singularity at $r = 0$, we assume a finite value of $r_{\text{in}} = 0.1 R$ in most cases. For the outer radius, we assume $r_{\text{out}} = 1000 R$. We restrict

ourselves to solving the equations in the first quadrant of the meridional plane, i.e., $0 \leq \theta \leq \pi/2$. This means that for dipolar fields, \overline{B}_θ is finite at the equator, while \overline{B}_r and \overline{B}_ϕ are vanishing. For quadrupolar fields, by contrast, \overline{B}_r and \overline{B}_ϕ are finite at equator, and \overline{B}_θ is vanishing. In terms of the components of $\overline{\mathbf{A}}$, we thus have the following boundary conditions on $\theta = \pi/2$ (Jabbari et al. 2015):

$$\frac{\partial \overline{A}_r}{\partial \theta} = \overline{A}_\theta = \frac{\partial \overline{A}_\phi}{\partial \theta} = 0 \quad (13)$$

for dipolar (odd parity) fields, and

$$\overline{A}_r = \frac{\partial \overline{A}_\theta}{\partial \theta} = \overline{A}_\phi = 0 \quad (14)$$

for quadrupolar (even parity) fields. In the radial direction, we adopt a perfect conductor boundary condition on both ends, i.e., $\overline{A}_\theta = \overline{A}_\phi = 0$. Owing to the use of the Weyl gauge, analogous boundary conditions in both directions also apply to the components of $\overline{\mathbf{E}}$.

In all our models, we use as initial condition weak Gaussian distributed noise for $\overline{\mathbf{A}}$. It acts as a seed magnetic field that is needed to allow the dynamo to amplify this field exponentially once α_0 is large enough. Owing to the $Q(\overline{\mathbf{B}})$ factor, the growth gets quenched and $|\overline{\mathbf{B}}|$ reaches values close to B_{eq} . The initial values of $\overline{\mathbf{E}}$ and $\overline{\mathbf{U}}$ are set to zero and \overline{p} is set to a constant reference value ρ_0 . We recall that gravity is not included in our models.

The strength of the α effect is quantified by the dynamo number $C_\alpha = \alpha_0 R / \eta_{\text{eff}}^{\text{int}}$. The diffusivity contrast is given by $C_\eta = \eta_{\text{eff}}^{\text{ext}} / \eta_{\text{eff}}^{\text{int}}$. Time is often expressed in terms of the diffusion time $\tau_{\text{diff}} = R^2 / \eta_{\text{eff}}^{\text{ext}}$ based on the exterior diffusivity. During the kinematic growth phase, the growth rate γ of the magnetic field is characterized by the nondimensional number $C_\gamma = \gamma R^2 / \eta_{\text{eff}}^{\text{int}}$. Unlike C_α and C_η , which are input parameters, C_γ is an output parameter.

For all of our spherical simulations, we use 8192×32 meshpoints in $r_{\text{in}} \leq r \leq 1000 R$ and $0 \leq \theta \leq \pi/2$. We use the PENCIL CODE (Pencil Code Collaboration et al. 2021), where the inclusion of the displacement current is facilitated by the module `special/disp_current.f90`. Its mean-field implementation through the module `magnetic/meanfield.f90` has been validated by reproducing $\gamma(k)$ from the dispersion relation for constant coefficients in the Cartesian case; see Appendix A. For earlier work with the PENCIL CODE in spherical geometry, where the mean-field momentum equation was included, we refer to the papers by Jabbari et al. (2015) and Jakab & Brandenburg (2021). In both papers, gravity played an important role, but in the present case, this

could lead to the development of a Parker wind, which we want to suppress in the present case. Therefore, we set here the gravitational potential to zero.

As an empirical measure of the front speed in simulations with the displacement current included, we determine the radius $r_{0.01}$ where the compensated value of the latitudinally averaged magnetic field has dropped to 0.01 times the value inside the magnetosphere. We expect that $r_{0.01}/ct < 1$ in all cases, which is indeed borne out by the simulations.

As already discussed in Ghosh et al. (2026), the front speed is constant during the kinematic growth phase. We call this growth ballistic. In the saturated state, the front speed decreases when the radius grows diffusively. Thus, for the front radius $r_*(t)$, we have

$$r_*^2(t) = \begin{cases} q_{\text{ballistic}} \gamma \eta_{\text{eff}}^{\text{ext}} (t - t_*)^2 & (\text{kinematic phase}), \\ q_{\text{diff}} \eta_{\text{eff}}^{\text{ext}} (t - t_*) & (\text{saturated phase}), \end{cases} \quad (15)$$

where $q_{\text{ballistic}}$ and q_{diff} are empirical coefficients of the order of unity and t_* denotes the time when the corresponding growth behavior is fully established.

2.3. Application to galactic scales

In this work, we present our results in dimensionless form by expressing length in units of R and time in units of $\tau_{\text{diff}} \equiv R^2/\eta_{\text{eff}}^{\text{ext}}$. In a specific example, Ghosh et al. (2026) estimated $\eta_{\text{eff}}^{\text{ext}} = 3000 \text{ kpc km s}^{-1}$. They presented their results in dimensionful fashion. The underlying dimensionless time at the end of their runs, $t_{\text{end}}/\tau_{\text{diff}}$, was about 1400. Identifying t_{end} with the Hubble time of 14 Gyr yields $\tau_{\text{diff}} = 0.01 \text{ Gyr}$. The unit of length is therefore $R = (\eta_{\text{eff}}^{\text{ext}} \tau_{\text{diff}})^{1/2} \approx 5.5 \text{ kpc}$. For one Hubble time, Ghosh et al. (2026) quoted a typical diffusion length of 200 kpc; see their Table II for a case they referred to as cosmic web dynamics.

We reiterate that our intention is not to provide a realistic model of a galactic dynamo. Instead, we are interested in understanding the far-field behavior of a generic dynamo. Our results may therefore in principle also be applicable to stellar dynamos. We stress that differential rotation is not included either. All these simplifications are done to keep the results simple enough to be able to identify potentially generic behaviors that are expected to occur in the far-field of astrophysical dynamos in general.

3. RESULTS

3.1. Exponential growth phase

Let us first look at the initial spreading of a dynamo-generated magnetic field into $r > R$. We adopt an α effect in $r_{\text{in}} \leq r \leq R$ with $C_\alpha = 25$, and a 10 or 50-fold increased value of η_{eff} in the exterior; see Table 1,

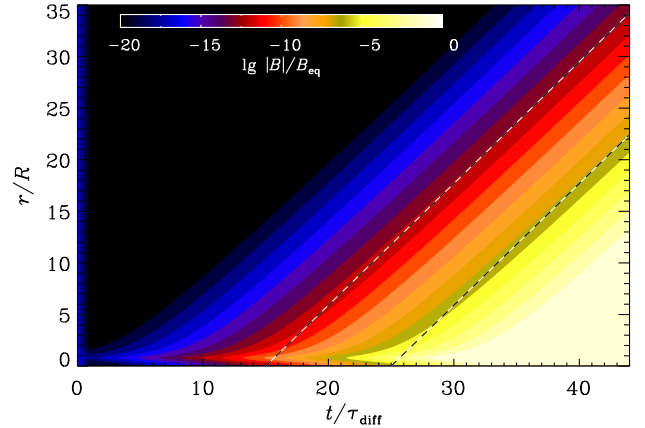


Figure 1. Colorscale representation of $\ln|\mathbf{B}|$ vs r and t for Run B. Yellow (blue) shades denote large (small) fields. The dynamo operates in $0 \leq r \leq 1$, as can be seen by the elevated field strength close to $r = 0$. The left (right) dashed line corresponds to $q_{\text{ballistic}} = 1$ with $t_*/\tau = 15$ (25).

where we present a summary of the runs discussed in this paper. The three runs of Ghosh et al. (2026) are presented in Table 1 as Runs A–C.

At early times, the magnetic field expands into $r > R$ and is found to fall off with distance like $e^{-\kappa r}$, where

$$\kappa = (\gamma/\eta_{\text{turb}})^{1/2} \quad (16)$$

is the radial decay rate, γ is the growth rate, and η_{turb} the turbulent magnetic diffusivity. This scaling is analogous to that for the skin effect, except that here we use an imaginary frequency, which leads to a non-oscillatory decay with increasing distance from the dynamo regime.

Since the magnetic field still increases exponentially like $e^{\gamma t}$, we have $B \sim e^{-\kappa r + \gamma t} = e^{-\kappa(r - c_{\text{front}}t)}$, where $c_{\text{front}} = \gamma/\kappa = (\gamma\eta_{\text{turb}})^{1/2}$ is the speed of the front, where we have used Equation (16). After some initial transient, the front radius begins to increase linearly with time; see Figure 1. This scaling is similar to that for the propagation of fronts of diseases (Murray et al. 1986). It also applies to the turbulent propagation of reactive fronts in combustion when the reaction speed is faster than diffusion (Brandenburg et al. 2011).

3.2. Magnetosphere radius

In Figure 2, we plot the latitudinally averaged root-mean-square magnetic field for dipolar and quadrupolar boundary conditions. For the quadrupolar case, we also compare with a case with a five times smaller magnetic diffusivity in the exterior. These three models were also discussed in Ghosh et al. (2026). It turns out that, during the early kinematic growth phase, the magnetic field grows and spreads similarly regardless of its hemispheric

Table 1. Summary of runs presented in the paper.

Run	sym	\bar{U}	cR/η_{eff}	r_{in}/R	h/R	m	C_α	C_η	C_γ	B_0/B_{eq}	q_{diff}^a	$r_{0.01}/ct^b$	n
A	D	$\neq 0$	∞	0.1	1	0	25	50	63	0.7	4.9	—	3
B	Q	$\neq 0$	∞	0.1	1	0	25	50	66	0.4	2.5	—	2
C	Q	$\neq 0$	∞	0.1	1	0	25	10	70	0.4	2.5	—	2
D	D	0	∞	0.1	1	0	25	1	74	0.7	4.9	—	3
E	D	0	1	0.1	1	0	25	1	7.2	0.7	—	0.8	3
F	D	0	0.5	0.1	1	0	25	1	3.7	0.7	—	0.6	3
G	Q	0	∞	0.1	1	0	25	1	77	0.4	2.5	—	2
G'	Q	0	∞	0.1	1	1	25	r^{-m}	68	0.4	2.5	—	2.16
G''	Q	0	∞	0.1	1	1.5	25	r^{-m}	68	0.4	2.5	—	2.23
H	Q	0	1	0.1	1	0	25	1	8.2	0.4	—	0.7	2
I	Q	0	0.5	0.1	1	0	25	1	4.2	0.4	—	0.6	2
J	Q	0	∞	0.2	1	0	50	1	386	0.6	2.5	—	2
K	Q	0	∞	0.1	0.5	0	50	1	348	0.2	2.5	—	2
L	Q	0	∞	0.1	0.2	0	50	1	78	2×10^{-5}	2.5	—	2

^aA hyphen indicates that Equation (17) does not provide an appropriate fit.

^bThe ratio $r_{0.01}/ct$ can only be evaluated when c is finite.

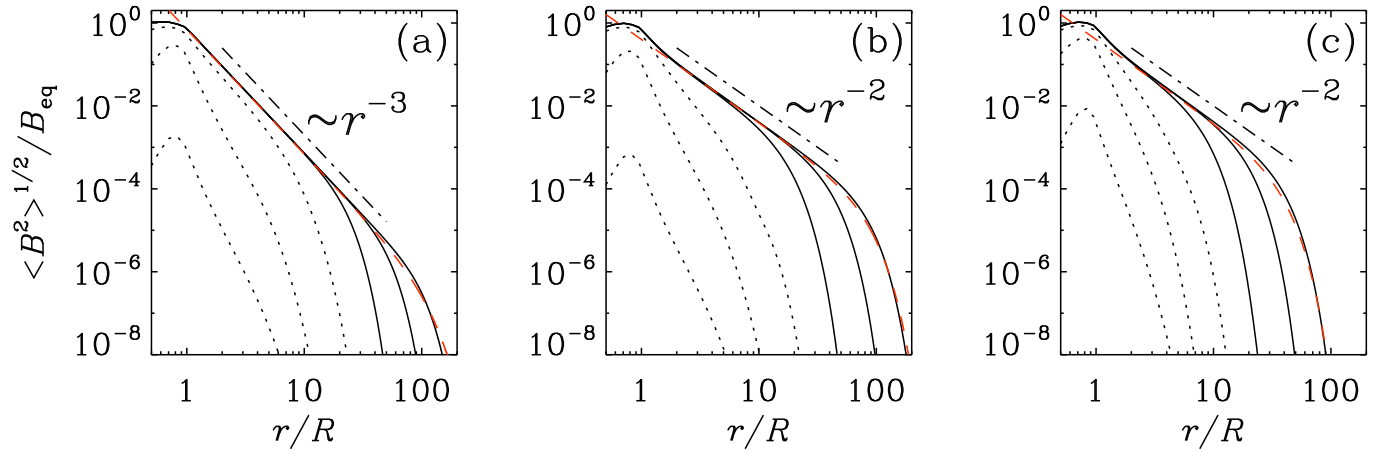


Figure 2. Radial dependence of $\langle B^2 \rangle^{1/2}$ at times $t/\tau_{\text{diff}} = 30, 35,$ and 50 (dotted lines), as well as $t/\tau_{\text{diff}} = 100, 300,$ and 1000 (solid lines), for (a) a dipolar field with $C_\eta = 50$ (Run A), (b) a quadrupolar field with $C_\eta = 50$ (Run B), and (c) a quadrupolar field with $C_\eta = 10$ (Run C). The asymptotic fall-offs $\propto r^{-3}$ for the dipolar field and $\propto r^{-2}$ for the quadrupolar fields are marked with dashed-dotted lines. The red lines denote the fit given by Equation (17) with the q_{diff} values listed in Table 1.

parity or the value of the exterior magnetic diffusivity. After the magnetic field has saturated in the dynamo-active part, it continues to spread like r^{-3} in the dipolar case, but like r^{-2} in the two quadrupolar cases. This can clearly be seen from Figure 2. Note also that, during the kinematic phase, the fields decay more rapidly with radius than during the saturated phase. Indeed, this is a transient behavior where the magnetic field changes from the exponential radial decay, $\propto e^{-\kappa r}$, to a power

law decay, $\propto r^{-n}$, in a shell around the dynamo, which then becomes the magnetosphere.

The radial powerlaw decay extends from the end of the dynamo-active part at $r = R$ to a radius $r_*(t)$ that we referred to as the front radius in Equation (15). It grows diffusively with time after some reference time t_* . This was already demonstrated by Ghosh et al. (2026) who referred to the sphere with radius $r_*(t)$ as the magnetosphere. For the nondimensional coefficient q_{diff} in Equation (15), the empirically determined value is close

to two—analogously to the law of Brownian diffusion (Einstein 1905). In Figure 2, we also compare the modulus of the latitudinally averaged magnetic field for the last time step, with a fit of the form

$$\bar{B}(r, t) = B_0 \left(\frac{r}{1 \text{ kpc}} \right)^{-n} \exp\left\{-\frac{1}{2}[r/r_*(t)]^2\right\}, \quad (17)$$

where B_0 characterizes the magnetic field strength inside the magnetosphere and n is the radial decay exponent. We find that the value of q_{diff} is around 4.9 for the dipolar configurations and around 2.5 for the quadrupolar configurations; see Table 1. This demonstrates that the radius of the magnetosphere scales with the exterior magnetic diffusivity, $\eta_{\text{turb}}^{\text{ext}}$, and is also independent of the diffusivity contrast, C_η . Even the case $C_\eta = 1$ results in the same scaling that is expected for the value $\eta_{\text{turb}}^{\text{ext}}$, which is then also equal to $\eta_{\text{turb}}^{\text{ext}}$ in that case.

Following Ghosh et al. (2026), we determine the instantaneous front radius $r_*(t)$ as a weighted integral,

$$r_*(t) = \int r^{n+1} \bar{B}(r, t) dr / \int r^n \bar{B}(r, t) dr. \quad (18)$$

The diffusive $r_*(t) \propto t^{1/2}$ scaling is confirmed for all runs where $\eta_{\text{eff}} = \text{const} = \eta_{\text{turb}}^{\text{ext}}$ in the exterior; see Run D, which is similar to Run A, and Run J, which is similar to Run B. The similarity between these pairs of runs also shows that neither the value of C_η nor the inclusion of feedback from the mean flow have a noticeable effect. Since the latter would work similarly to the aforementioned magneto-frictional approach, we conclude that our magnetic fields are already nearly force-free.

3.3. Radially varying diffusivity

The local front speed depends on the value of η_{eff} . When it is a function of r , the front speed can increase at locations where η_{eff} is larger. Thus, if we have a radially increasing profile, i.e., $m > 0$ in Equation (12), we expect the front speed to increase with r . This is demonstrated in Figure 3, where we compare $r_*(t)$ for Runs G' and G'' with $m = 1$ and 1.5 with the case $m = 0$. Here, we have used $r_0/R = 10$ in Equation (12). For large radii, we find that the temporal growth is steeper: $\propto t^{0.8}$ for $m = 1$ and $\propto t^{1.3}$ for $m = 1.5$. However, the shallow inversely quadratic radial fall-off of the mean magnetic field for the quadrupolar field is still approximately obeyed. In Appendix B, we demonstrate that an accurate measurement yields slightly steeper radial decays with $n \approx 2.16$ and 2.23 for models with $m = 1$ and 1.5, respectively.

The temporal scalings of $r_*(t)$ for different values of m give an approximate idea about the sensitivity. We see that the lines remain still somewhat curved, so there is

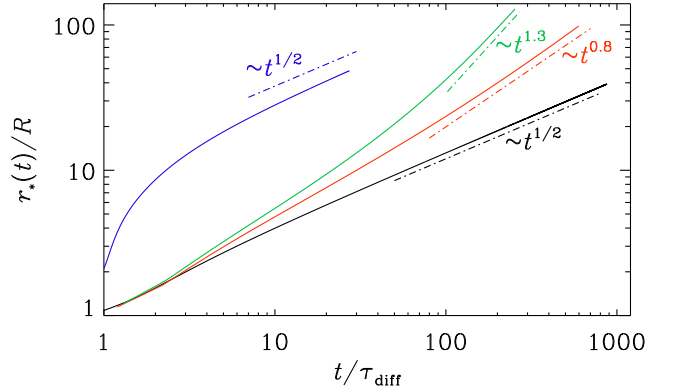


Figure 3. Comparison of $r_*(t)$ for Runs B (blue), G (black), G' (red), and G'' (green).

no true powerlaw scaling. If the turbulent magnetic diffusivity outside the galaxy were to be highly variable, we might expect a corrugated magnetosphere. Conversely, if the magnetosphere is not strongly corrugated, it would indicate a more nearly constant distribution of r_* . In either case, however, the spatial scaling of the magnetic field within the magnetosphere would still remain approximately $\propto r^{-2}$ for the quadrupolar configuration.

3.4. Comments on nonuniform diffusive scalings

It is tempting to refer to a diffusive scaling as one that scales like $t^{1/2}$ with time. Conversely, one might refer to departures from such as scaling as nondiffusive. This is however misleading, because the expansion speed is still limited by the local magnetic diffusivity. We can see this by inserting Equation (12) into Equation (15) for the saturated phase, and assuming $r \gg r_0$, which yields

$$r_*(t)/r_0 \approx [q_{\text{diff}} \eta_{\text{eff}}^{\text{ext}} (t - t_*)/r_0^2]^{1/(2-m)}. \quad (19)$$

Thus, if correct, we might asymptotically expect a temporal growth $\propto t$ for $m = 1$ (instead of the numerically obtained $t^{0.8}$ behavior) and $\propto t^2$ for $m = 1.5$ (instead of $t^{1.3}$). This departure is consistent with the fact that the lines in Figure 3 were still somewhat curved and that there was no true powerlaw scaling.

We emphasize that the accelerated expansion would not affect our conclusion that magnetic fields cannot significantly extend into the voids. This would require unreasonably large amounts of turbulence in the voids. We return to this point later in this paper when we compare more quantitatively with the vacuum case.

3.5. Radial power law scaling within the magnetosphere

To study the radial power laws for the dipolar and quadrupolar configurations in more detail, we now express the latitudinal dependence in terms of Legendre

polynomials. An axisymmetric magnetic field can be written as (Moffatt 1978; Parker 1979; Krause & Rädler 1980)

$$\overline{\mathbf{B}} = \hat{\phi}\overline{B}_\phi + \nabla \times \hat{\phi}\overline{A}_\phi, \quad (20)$$

where $\overline{A}_\phi(r, \theta, t)$ and $\overline{B}_\phi(r, \theta, t)$ are independent of each other outside the dynamo region and characterize the poloidal and toroidal magnetic field decay in the radial direction. They can be expanded as¹

$$\overline{A}_\phi = \sum a_\ell(r) P_\ell^1(\cos \theta), \quad \overline{B}_\phi = \sum b_\ell(r) P_\ell^1(\cos \theta). \quad (22)$$

Dipolar (quadrupolar) magnetic fields have odd (even) ℓ in $a_\ell(r)$ and even (odd) ℓ in $b_\ell(r)$.

We compute the coefficients $a_\ell(r)$ and $b_\ell(r)$ from our simulations as

$$a_\ell(r) = N_\ell \int \overline{A}_\phi(r, \theta) P_\ell^1(\cos \theta) d \cos \theta, \quad (23)$$

$$b_\ell(r) = N_\ell \int \overline{B}_\phi(r, \theta) P_\ell^1(\cos \theta) d \cos \theta, \quad (24)$$

where $N_\ell = (2\ell + 1)(\ell - 1)!/(\ell + 1)!$ is a normalization factor. In particular, $N_1 = 3/2$ and $N_2 = 5/6$. In Figure 4, we plot the radial dependences of $a_{11}(r)$ and $b_{21}(r)$ for the dipole and of $a_{21}(r)$ and $b_{11}(r)$ for the quadrupole. We clearly see the asymptotic slopes $a_{11} \propto r^{-2}$ and $b_{21} \propto r^{-3}$ for the dipole and $b_{11} \propto r^{-2}$ and $a_{21} \propto r^{-3}$ for the quadrupole.

Note that for the dipolar and quadrupolar solutions, the roles of A_ϕ and B_ϕ are interchanged; see Figure 4. In particular, the r^{-2} behavior for \overline{A}_ϕ of the dipole is now seen for the \overline{B}_ϕ field of the quadrupole, and the r^{-3} behavior for \overline{B}_ϕ of the dipole is now seen for the \overline{A}_ϕ field of the quadrupole. Thus, although the poloidal component for a quadrupolar configuration still decays like r^{-4} , the toroidal component \overline{B}_ϕ for this quadrupolar configuration decays like \overline{A}_ϕ for the dipolar configuration, i.e., like r^{-2} .

In the following, we discuss the individual components of the magnetic field in more detail. The two components of the poloidal field are given by $B_r = D_\theta A_\phi$ and $B_\theta = -D_r A_\phi$, where $D_\theta = r^{-1} \sin^{-1} \theta \partial_\theta (\sin \theta \cdot)$, and $D_r = r^{-1} \partial_r (r \cdot)$ are differential operators.

¹ In general, axisymmetric and nonaxisymmetric magnetic fields can be written as

$$\overline{\mathbf{B}} = \nabla \times r\mathbf{T} + \nabla \times \nabla \times r\mathbf{S}, \quad (21)$$

where $T(r, \theta, \phi, t)$ and $S(r, \theta, \phi, t)$ are the superpotentials for the three-dimensional toroidal and poloidal fields, respectively. In axisymmetry, this implies that $B_\phi = -\partial T/\partial \theta$, and if $T(r, \theta) = P_\ell(\cos \theta)$, then $B_\phi = -P_\ell^1(\cos \theta)$. Likewise, using $A_\phi = -\partial S/\partial \theta$, and if $S(r, \theta) = P_\ell(\cos \theta)$, then $A_\phi = -P_\ell^1(\cos \theta)$.

3.6. Lowest-order dipole

Employing our lowest-order dipole approximation, we find the two fields to be proportional to

$$\overline{A}_\phi = a_D r^{-2} P_1^1(\cos \theta), \quad \overline{B}_\phi = b_D r^{-3} P_2^1(\cos \theta). \quad (25)$$

Therefore, since $P_1^1(\cos \theta) = -\sin \theta$ and $P_2^1(\cos \theta) = \cos \theta$, we have

$$\overline{B}_r = -2a_D r^{-3} \cos \theta \equiv -2a_D r^{-3} P_1(\cos \theta), \quad (26)$$

$$\overline{B}_\theta = -a_D r^{-3} \sin \theta \equiv a_D r^{-3} P_1^1(\cos \theta). \quad (27)$$

For our model, we find $a_D \approx 0.20 B_{\text{eq}} R^3$ and $b_D \approx 0.60 B_{\text{eq}} R^3$.

3.7. Lowest-order quadrupole

Our lowest-order quadrupole is proportional to

$$\overline{A}_\phi = a_Q r^{-3} P_2^1(\cos \theta), \quad \overline{B}_\phi = b_Q r^{-2} P_1^1(\cos \theta). \quad (28)$$

Since $P_2^1(\cos \theta) = -3 \sin \theta \cos \theta$ and $P_2(\cos \theta) = (3 \cos^2 \theta - 1)/2$, we have

$$\overline{B}_r = 3a_Q r^{-4} (1 - 3 \cos^2 \theta) \equiv -6a_Q r^{-4} P_2(\cos \theta), \quad (29)$$

$$\overline{B}_\theta = -6a_Q r^{-4} \sin \theta \cos \theta \equiv 2a_Q r^{-4} P_2^1(\cos \theta). \quad (30)$$

For our model, we find $a_Q \approx 0.09 B_{\text{eq}} R^4$ and $b_Q \approx 0.49 B_{\text{eq}} R^2$.

3.8. Current density profiles

Next, we compute $\mu_0 \overline{\mathbf{J}} = \nabla \times \overline{\mathbf{B}}$, which is given by

$$\mu_0 \overline{\mathbf{J}} = \hat{\phi} \mu_0 \overline{J}_\phi + \nabla \times \hat{\phi} \overline{B}_\phi, \quad (31)$$

where

$$\mu_0 \overline{J}_\phi = -(\mathcal{D}_r^2 + \mathcal{D}_\theta^2) \overline{A}_\phi, \quad (32)$$

is proportional to the toroidal current density. Again, $\mathcal{D}_r^2 \equiv D_r D_r$ and $\mathcal{D}_\theta^2 \equiv d_\theta D_\theta$ with $d_\theta = r^{-1} \partial_\theta$ are convenient shorthands.

For the lowest-order dipole with $A_\phi = a_D r^{-2} P_1^1(\cos \theta)$, we have

$$\mathcal{D}_r^2(-r^{-2} \sin \theta) = -2r^{-4} \sin \theta \quad (33)$$

and

$$\mathcal{D}_\theta^2(-r^{-2} \sin \theta) = 2r^{-4} \sin \theta, \quad (34)$$

and therefore $\overline{J}_\phi = 0$. Thus, we have $\mu_0 \overline{\mathbf{J}} = \nabla \times \hat{\phi} \overline{B}_\phi$, and therefore the Lorentz force, $\overline{\mathbf{J}} \times \overline{\mathbf{B}}$, is

$$\overline{\mathbf{J}} \times \overline{\mathbf{B}} = (\nabla \times \hat{\phi} \overline{B}_\phi) \times (\hat{\phi} \overline{B}_\phi + \nabla \times \hat{\phi} \overline{A}_\phi) / \mu_0, \quad (35)$$

and has only a purely toroidal component, whose divergence vanishes. Therefore, such a field is nearly force-free, except for the ϕ component, which only drives a

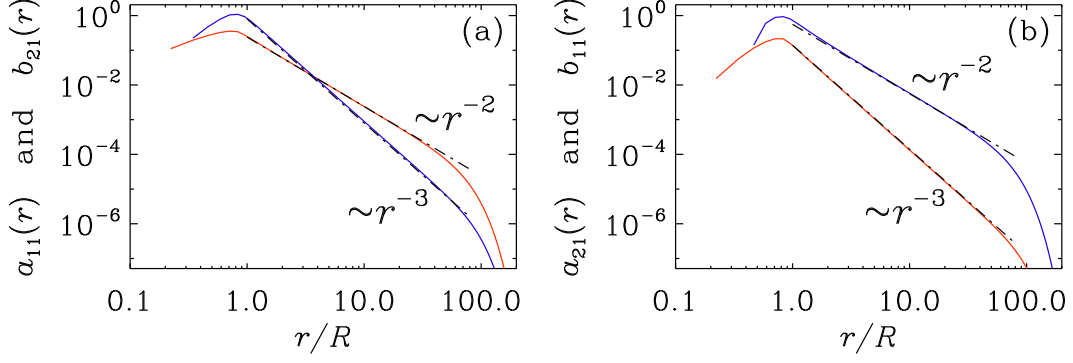


Figure 4. Radial dependence of (a) $a_{11}(r)$ and $b_{21}(r)$ for the dipole (Run A) and (b) $a_{21}(r)$ and $b_{11}(r)$ for the quadrupole (Run B). The asymptotic slopes are $a_{11}/(B_{\text{eq}}R) \approx 0.052 (r/R)^{-2}$ and $b_{21}/B_{\text{eq}} \approx 0.3 (r/R)^{-3}$ for the dipole and $b_{11}/B_{\text{eq}} \approx 0.132 (r/R)^{-2}$ and $a_{21}/(B_{\text{eq}}R) \approx 0.037 (r/R)^{-3}$ for the quadrupole, and are marked with dashed-dotted lines. For a vacuum field, b_{11} would be zero. The red and blue lines give the scalings of \bar{A}_ϕ and \bar{B}_ϕ , respectively, which are opposite for the dipolar and quadrupolar cases.

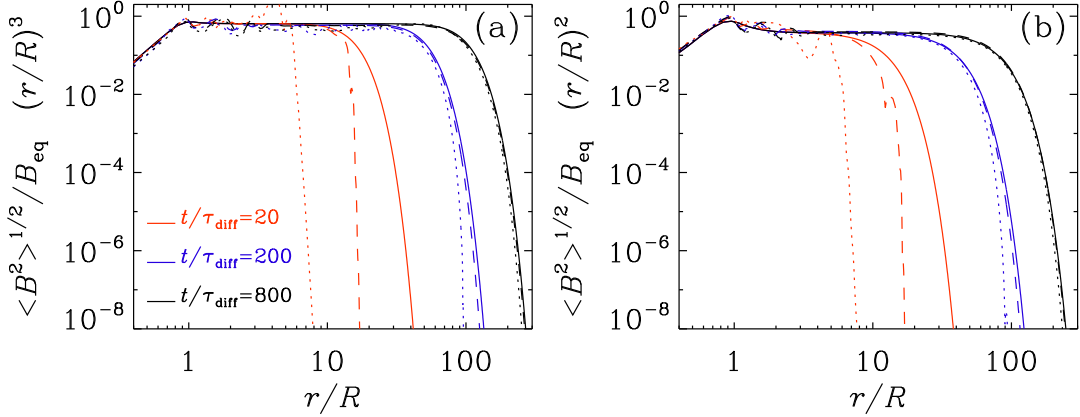


Figure 5. Radial magnetic field profiles compensated (a) by r^3 for the dipolar case (Runs D–F), and (b) by r^2 for the quadrupolar case (Run G–I). For the solid lines, the displacement current is neglected (Runs D and G), while for the dashed and dotted lines it is included with $cR/\eta_{\text{eff}} = 1$ (Runs E and H) and 0.5 (Runs F and I), respectively. The red, blue, and black lines correspond to the times $t/\tau_{\text{diff}} = 20$, 200, and 800.

rotational motion. This agrees with our conclusion at the end of Section 3.2.

For the quadrupole with $\bar{A}_\phi \propto r^{-3} \sin \theta \cos \theta$, we have

$$D_r^2 r^{-3} = 6 r^{-5} \quad (36)$$

and

$$D_\theta^2 \sin \theta \cos \theta = -6 r^{-2} \sin \theta \cos \theta. \quad (37)$$

Therefore, again, $\bar{J}_\phi = 0$.

For the quadrupole, we have

$$D^2 \bar{B}_\phi = 0, \quad (38)$$

similarly to \bar{A}_ϕ for the dipolar field. However, unlike for \bar{A}_ϕ , where $D^2 \bar{B}_\phi = \mu_0 \bar{J}_\phi$ is the toroidal current density, in the case of a quadrupolar field, $D^2 \bar{B}_\phi$ has no physically obvious meaning. What is more relevant in a

conductor is the Lorentz force, $\bar{\mathbf{J}} \times \bar{\mathbf{B}}$, which has poloidal and toroidal components. Its toroidal component coming from the poloidal components $\bar{\mathbf{J}}_{\text{pol}}$ and $\bar{\mathbf{B}}_{\text{pol}}$ is non-vanishing, but it only leads to driving an azimuthally differential rotation, and becomes extremely weak owing to its fast radial decay $\propto r^{-5}$. The poloidal Lorentz force has the components $\bar{\mathbf{J}}_{\text{pol}} \times \bar{\mathbf{B}}_\phi \hat{\phi}$ and $\hat{\phi} D^2 \bar{A}_\phi \times \bar{\mathbf{B}}_{\text{pol}}/\mu_0$. Using $\mu_0 \bar{\mathbf{J}}_{\text{pol}} = \nabla \times \bar{\mathbf{B}}_\phi \hat{\phi}$ and $\bar{\mathbf{B}}_{\text{pol}} = \nabla \times \bar{A}_\phi \hat{\phi}$, we have $(\nabla \times \bar{\mathbf{B}}_\phi \hat{\phi}) \times \bar{\mathbf{B}}_\phi \hat{\phi} = -\varpi^{-1} \nabla(\varpi \bar{B}_\phi^2)$, and it leads to a radial force that falls off very rapidly like r^{-5} . Thus, except for a term $\bar{B}_\phi^2 \nabla \ln \varpi^2$, the Lorentz force can in principle be balanced by a pressure gradient. The residual $\bar{B}_\phi^2 \nabla \ln \varpi^2$ term, on the other hand, can be balanced by the centrifugal force. In that sense, our quadrupolar configuration is nearly force-free.

As already stated above, outside the dynamo region, \overline{A}_ϕ and \overline{B}_ϕ act independently of each other, and each component is subject to diffusion. Thus, unlike the dynamo interior, where \overline{B}_ϕ is coupled to \overline{A}_ϕ by induction effects such as differential rotation, it is here expanding just because of (turbulent) magnetic diffusion and can therefore adopt the same behavior as \overline{A}_ϕ . In the present case, this means that for the quadrupolar configuration, $\overline{B}_\phi \propto r^{-2}$, just like the $\overline{A}_\phi \propto r^{-2}$ behavior for the dipolar configuration.

3.9. Effects of the displacement current

As we have seen from the Cartesian simulations in Appendix A, the inclusion of the displacement current can lead to a smaller growth rate γ ; see Appendix A. It also can only decrease the front speed, $c_{\text{front}} = \gamma/\kappa$. As a consequence, it turns out that the front speed is always less than the speed of light.

As alluded to in the introduction, the values of the magnetic diffusivity would need to be extremely large if one wanted to emulate the conditions of a vacuum. In vacuum, an electromagnetic wave propagates at the speed $c = 300,000 \text{ km s}^{-1}$, which implies a propagation distance $L = ct_{\text{H}} \approx 5 \text{ Gpc}$ in one Hubble time, $t_{\text{H}} \approx 14 \text{ Gyr}$. This corresponds to a reference diffusivity of about $\eta_{\text{ref}} \equiv L^2/t_{\text{H}} = c^2 t_{\text{H}} \approx 2 \times 10^{12} \text{ kpc km s}^{-1}$, which is nearly 10^9 times larger than the value $\eta_{\text{turb}} = 3000 \text{ kpc km s}^{-1}$ used by Ghosh et al. (2026). Such large values are unrealistic.² Nevertheless, it is of interest to see how the spherical expansion of the magnetic field is affected by the finite speed of light in a medium of such an extremely large magnetic diffusivity. In the following, we consider the values $cR/\eta_{\text{ref}} = 1$ and 0.5 . Again, these ratios are chosen to be unrealistically small. This is done just to see the qualitative and quantitative effects of including the Faraday displacement current. Again, we choose $C_\eta = 1$, which, as demonstrated above, does not affect the radial expansion behavior compared to cases with larger values of C_η . The results for our models in spherical geometry are shown in Figure 5. For these models, we have neglected the evolution of the mean flow, i.e., we only solve Equations (5) and (6). It turns out that only at early times, the solution is noticeably affected by the finite speed of light—even for $cR/\eta_{\text{eff}} = 0.5$. In these cases, as explained in Section 2.2, we characterize the front radius by the radius $r_{0.01}$, where the compensated magnetic field has dropped to 0.01 times the value inside the magnetosphere. We

see from Table 1 that $r_{0.01}/ct < 1$ is obeyed in all cases with finite values of cR/η_{eff} . This ratio varies between 0.8 and 0.6 for our dipolar configurations (Runs E and F) and between 0.7 and 0.6 (Runs H and I) for our quadrupolar configurations. Thus, $r_{0.01}$ is close to but always less than the Hubble radius.

3.10. Effects of changing r_{in} and h

In Figure 6, we examine the effects of varying the ratios r_{in}/R and h/R (Runs J–L). To ensure that the dynamo remains excited in spite of its smaller volume, we have here also increased the value of C_α from 25 to 50. We see that the radial fall-off is basically unchanged when increasing the value of r_{in}/R from 0.1 (Run G) to 0.2 (Run J). By contrast, when decreasing the value of h/R from 1 (Run G) to 0.5 (Run K) and 0.2 (Run L), we see that the radial profiles become more complicated and develop radial oscillations. In addition, there is even an indication of a drop of the magnetic field in the wake of the front. To see this more clearly, we run the case with $h/R = 0.2$ for a much longer time. The results suggests that the magnetic field takes the form of an azimuthal ring or at least a shell instead of a filled sphere. This complication would have obscured the otherwise simple radial powerlaw behaviors discussed above. This was also the reason why we have focussed our study mostly on the case $H/R = 1$. It is important to note, however, that the position of the exponential drop at the edge of the magnetosphere is unchanged, as is seen by the unchanged value of the parameter q_{diff} listed in Table 1 and the fits presented in Figure 6 for the last time step.

4. OBSERVATIONAL IMPLICATIONS

To make contact with observations, Ghosh et al. (2026) computed the rotation measure (RM). Assuming a radial powerlaw dependence for the thermal electron density, $n_{\text{th}} \propto r^{-s_{\text{th}}}$, they found that RM falls off with radius like $r^{-2-s_{\text{th}}}$ for the dipolar solution and like $r^{-1-s_{\text{th}}}$ for the quadrupolar solution. Measuring such radial profiles can help to verify our expected scalings.

Another observational diagnostic is the resulting synchrotron emission. The synchrotron intensity $I(x, z, \lambda)$ and the complex polarization, $\mathcal{P}(x, z, \lambda) \equiv Q + iU$ are obtained by line-of-sight integration. Here, Q and U are the Stokes parameters characterizing linear polarization and λ is the wavelength.

To get an idea about the basic properties of I , Q , and U , we adapt the expression for the radial scaling of the magnetic field given by Equation (17) to the lowest order dipole and quadrupole configurations of Sections 3.6 and 3.7. We then compute the components

$$\overline{B}_x = \sin \theta \cos \phi \overline{B}_r + \cos \theta \cos \phi \overline{B}_\theta - \sin \phi \overline{B}_\phi, \quad (39)$$

² Even if the turbulent velocity was equal to the speed of light, it would require a correlation length of more than 70 Gpc to reach a turbulent diffusivity of $10^{12} \text{ kpc km s}^{-1}$.

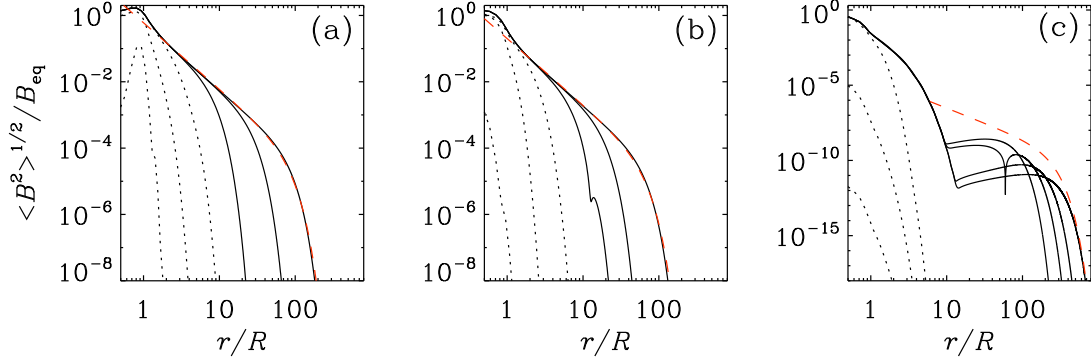


Figure 6. Radial magnetic field profiles for Runs J, K, and L. For Run J, we have $r_{\text{in}}/R = 0.2$ instead of 0.1, while for Runs K and L, we have $h/R = 0.5$ and 0.2 , respectively. The times are (a) $t/\tau_{\text{diff}} = 0.1, 0.3, 1.5$ for the dotted lines and $10, 100, 942$ for the solid lines, (b) $0.1, 0.2, 0.8$ for the dotted lines and $10, 50, 530$ for the solid lines, (c) $0.2, 0.4, 0.6$ for the dotted lines and $500, 1200, 2700, 5990$ for the solid lines.

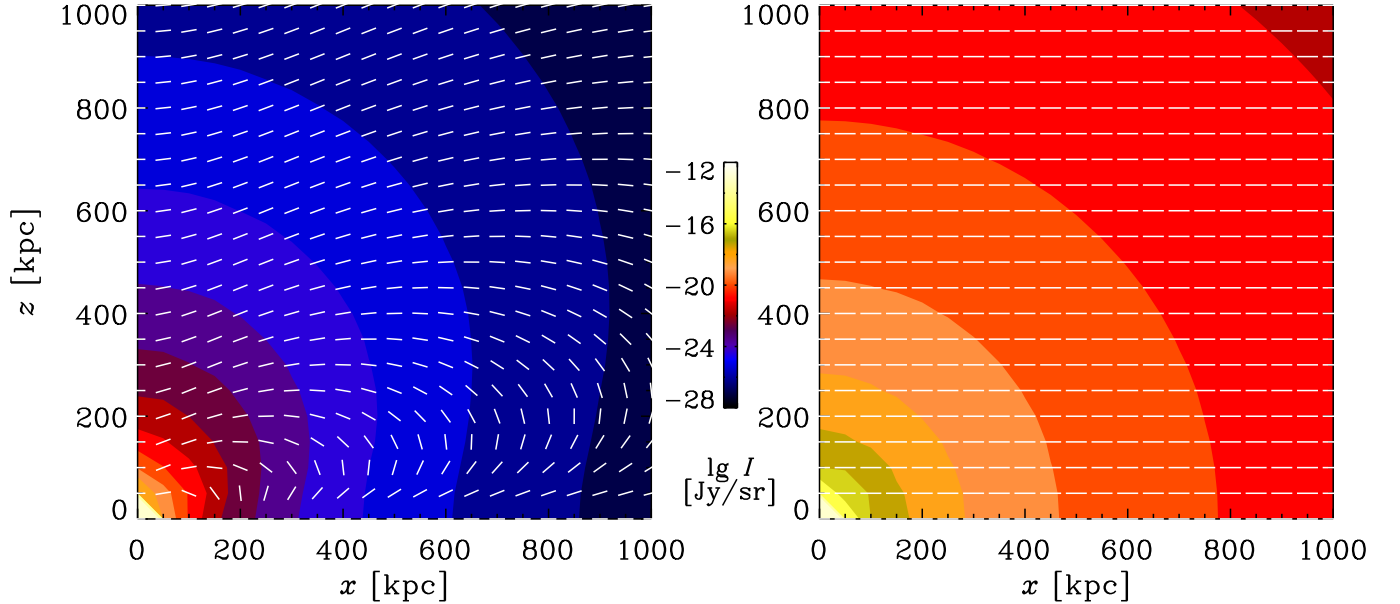


Figure 7. Polarization vectors (Q, U) superimposed on a color scale representation of the logarithmic intensity $I(x, z)$ (in Jy/sr) for Runs A (dipolar configuration, left) and B (quadrupolar configuration, right).

$$\overline{B}_z = \cos \theta \overline{B}_r - \sin \theta \overline{B}_\theta, \quad (40)$$

in Cartesian coordinates where ϕ is the azimuthal angle and θ is the colatitude. The synchrotron intensity $I(x, z)$ projected onto the xz plane is given by

$$I(x, z, \lambda) = \int_{-L}^L \epsilon(x, y', z, \lambda) dy', \quad (41)$$

where $\epsilon \propto n_{\text{CR}} \overline{B}_\perp^{(\zeta+1)/2} \lambda^{(\zeta-1)/2}$ is the emissivity, n_{CR} is the cosmic ray density, λ is the wavelength, and ζ is the spectral index of the momentum distribution (Ginzburg & Syrovatskii 1965). Realistic values for ζ are in the range 2.8–3.2 as a result of the combi-

nation of the continuous injection of secondary electrons (by hadronic collisions), the injection of primary electrons by supernova-driven shocks, and the modulation by energy-dependent diffusion (e.g., Beck 1991; Werhahn et al. 2021; Armillotta et al. 2025). Here, for simplicity, we use $\zeta = 3$, because then we have $\epsilon \propto \overline{B}_\perp^2$ and the complex intrinsic polarization is simply proportional to B_\perp^2 , where $B_\perp = \overline{B}_x + i\overline{B}_z$ is the complex magnetic field in the plane of the sky; see Brandenburg & Stepanov (2014) for earlier work utilizing this formalism.

We ignore here the effects of Faraday rotation, which would have introduced a factor $\exp(2i\phi\lambda^2)$ un-

der the integral of \mathcal{P} , on the basis that we showed already in Ghosh et al. (2026) that this is negligible but in the galaxy core. Here, $\phi(x, y, z) = -K \int_0^y (n_{\text{th}} \overline{B}_y)(x, y', z) dy'$ is the Faraday depth and K is a known constant. Neglecting Faraday rotation corresponds to taking the limit $\lambda \rightarrow 0$.

In Figure 7, we present synthetic maps of the synchrotron intensity $I(x, z)$ for the same dipolar and quadrupolar configurations as in Ghosh et al. (2026), corresponding to Runs A and B, respectively. For n_{CR} , we assume for simplicity a steady radial profile similarly to n_{th} , which we write here as $n_{\text{CR}} \propto r^{-s_{\text{CR}}}$, analogously to the expression for n_{th} used by Ghosh et al. (2026). Here, we simply assumed $s_{\text{CR}} = 1$, although it should be noticed that radiative losses may complicate this trend in reality (e.g., Peron et al. 2021; Pfrommer et al. 2022; Armillotta et al. 2025). To have a quantitative estimate of the magnetospheric emission, we used (Rybicki & Lightman 1986, see also Appendix C)

$$\epsilon \, dy \approx \frac{5 \, \mu\text{Jy}}{\text{sr}} \left(\frac{n_{\text{CR}}^{(100 \text{ kpc})}}{10^{-7} \text{ cm}^{-3}} \right) \left(\frac{B_{\text{eq}}}{1 \, \mu\text{G}} \right)^2 \left(\frac{\lambda}{2 \text{ m}} \right) \left(\frac{dy}{1 \text{ kpc}} \right), \quad (42)$$

where $n_{\text{CR}}^{(100 \text{ kpc})}$ is the cosmic ray density at a galactocentric distance of 100 kpc, assuming that $s_{\text{CR}} = 1$ may still be valid at that distance, which depends on the long-term integrated dispersal of cosmic rays around galaxies and in large-scale structures (see e.g. Vazza et al. 2025, for recent numerical studies).

In Figure 7, we overlay the polarization vectors (Q, U). For a powerlaw dependence of the cosmic ray number density, $n_{\text{CR}} \propto r^{-s_{\text{CR}}}$, assuming $\overline{B}_\perp \propto r^{-n}$ with $n = 2$ for quadrupoles and $n = 3$ for dipoles, the intrinsic emissivity becomes proportional to $n_{\text{CR}} \overline{B}_\perp^2 \propto r^{-s_{\text{CR}} - 2n}$, see Equation (17). Line-of-sight integration adds another power, yielding $r^{-s_{\text{CR}} - 2n + 1}$. Thus, for quadrupolar (dipolar) configurations, we find $I \propto r^{-3 - s_{\text{CR}}}$ ($\propto r^{-5 - s_{\text{CR}}}$).

We see that the polarization vectors are predominantly in the x direction. This is a commonly observed feature related to the dominance of the toroidal magnetic field; see, e.g., Brandenburg et al. (1993) and Elstner et al. (1995) for earlier work where, unlike the present case, a radial wind was included. It is only for the dipolar configuration that the toroidal field changes sign at the midplane. This causes clear departures from the otherwise nearly perfect alignment of the polarization vectors with the x direction.

As expected, the radial fall-off of the synchrotron intensity is still rather steep—even for the quadrupolar configuration. Let us therefore now discuss whether

our models of intensity distributions could be observed in real galaxies. For example, an 8 hour integration with the LOFAR High Band Antenna (HBA) at ≈ 150 MHz typically reaches a noise level of $3\sigma_{\text{rms}} \approx 1 \, \mu\text{Jy}/\text{arcsec}^2 = 2.35 \cdot 10^{-17} \text{ Jy}/\text{sr}$. Based on Figure 7, a fraction of the expected radio emission should be detectable in both cases by radio telescopes, yet in the dipolar configuration the detectable region should be confined within a ≤ 200 kpc radius, while in the quadrupolar case a much larger region should be detectable. However, for a quantitative prediction one also needs to fix the radial distribution of cosmic rays, which can only roughly be guessed at this stage, while in real galaxies it must be affected by the presence of large-scale outflows, especially at larger radii where the inertia of cosmic rays is expected to become dynamically dominant (e.g., Chiu et al. 2024). Interestingly, however, the differences in the orientation of polarization vectors is rather independent of the distribution of relativistic electrons. On the other hand, the orientation of polarization vectors might provide more immediate ways of testing the large-scale distribution of magnetic fields. Intriguingly, preliminary work using LOFAR observations may already have yielded results that are possibly consistent with our predictions of a finite magnetosphere (Oei 2025).

Whether the magnetosphere is caused by a galactic wind or by turbulent magnetic diffusion cannot be easily distinguished. Both would lead to the same r^{-2} flux-conserving radial decay. However, the combination of spectral and polarimetric observations at large radii have been shown to provide a sensitive way to test the presence of (re)acceleration processes of cosmic rays (e.g., Taziaux et al. 2025). Those cosmic rays are expected in the case of outflows (e.g., Chiu et al. 2024), but not necessarily in the case of the extended magnetosphere studied in this work.

5. CONCLUSIONS

We have studied the radial spreading of a dynamo-generated magnetic field into its electrically conducting surroundings. Unlike conventional dynamo theory, where the exterior field is assumed to be a current-free potential field, ours has electric currents and is only approximately force-free. As already reported by Ghosh et al. (2026), the quadrupolar field has a toroidal component, that decays with radial distance only like r^{-2} , which is slower than the r^{-3} decay of the poloidal component for the dipolar configuration in the far-field of the dynamo. We are not aware of earlier reports of such a slow radial magnetic field decay.

An important difference compared to earlier work on force-free magnetic fields in the dynamo exterior, lies in the fact that we study the time-dependent case with direct numerical simulations, where a nearly force-free field is only gradually building up in an electrically conducting environment. As far as the formulation of the effective boundary condition of the dynamo is concerned, which was the main purpose of considering force-free exteriors (Bonanno 2016; Bonanno & Del Sordo 2017), the limited time available in establishing the exterior field may not be very important on such short length scales. However, the slower radial decay and the sharp exponential fall-off marking the end of the magnetosphere may be of observational interest (Ghosh et al. 2026) and might be tested with the new generation of radio observatories (e.g., Ghasemi-Nodehi et al. 2022). This feature could be used to distinguish the field from a dipolar one, on the one hand, and from one governed by a wind, on the other. Such winds have indeed frequently been discussed in simulations (Aramburo-García et al. 2021, 2022; Bondarenko et al. 2022), including cases with a dynamo coupled either an imposed wind (Brandenburg et al. 1993) or to a dynamically sustained one (Perri et al. 2021; Jakab & Brandenburg 2021).

In the work of Brandenburg et al. (1993), maps of synchrotron emission were presented, but the displayed results do not allow us to determine whether the radial fall-off is characterized by a power law. Jakab & Brandenburg (2021) did not compute synchrotron emission, but they presented their results for \overline{B}_ϕ by compensating them by r^2 . This shows that, although their field configuration was dipolar, the presence of a wind alone can also lead to a slow radial decay of \overline{B}_ϕ .

In the present cases, an important clue in understanding the origin of the r^{-2} decay of \overline{B}_ϕ comes from the correspondence between the pair $(\overline{B}_\phi, \overline{A}_\phi)$ for a quadrupolar configuration and the pair $(\overline{A}_\phi, \overline{B}_\phi)$ for a dipolar configuration. In both cases, the residual decays are of the form

$$\left. \begin{array}{l} (\overline{B}_\phi, \overline{A}_\phi) \\ (\overline{A}_\phi, \overline{B}_\phi) \end{array} \right\} = [r^{-2} P_1^1(\cos \theta), r^{-3} P_2^1(\cos \theta)], \quad (43)$$

and their evolution is simply the result of diffusion. Unlike the action of α and Ω effects in the dynamo interior, diffusion does not couple \overline{A}_ϕ and \overline{B}_ϕ . This is why the aforementioned correspondence is possible.

While these results are also borne out in cases where the displacement current is included, we have shown that it can safely be ignored in all cases of interest. Its main role lies in limiting the expansion speed in poorly

conducting media rather than facilitating a radial expansion.

It is also interesting to note that the far-field magnetic field configurations are nearly force-free in the sense that the resulting Lorentz force can be balanced by pressure gradient and centrifugal forces. However, this aspect may well be subdominant because the radial fall-off of the Lorentz force is rapid and our results are essentially independent of whether the momentum equation is included in our simulations.

In the present work, we have made a number of simplifying assumptions that has helped producing clean results. In particular, the assumption of a spherical rather than an oblate dynamo geometry have helped in producing powerlaw behaviors of the radial magnetic field decay. It is possible that at large distances from the dynamo region, this assumption becomes less critical. However, the present results for oblate dynamo geometries rather suggest that magnetosphere may take the form of a ring or a spherical shell. The inclusion of differential rotation in the dynamo region would complicate the results further. Preliminary studies have shown that the r^{-2} fall-off for the quadrupolar configuration might become steeper. It is unclear, however, how this changes at larger distances. Further modifications are expected if we allowed for a radial wind to develop. In that case, however, it is conceivable that one might find results that depend on the activity of the galaxy in driving such a wind. Nevertheless, a slow radial fall-off for quadrupolar fields may still survive under certain more realistic conditions. As explained above, the resulting synchrotron emission may be of observational interest. However, as already stressed by Ghosh et al. (2026), the radii of galactic magnetospheres are not affected by this and remain prohibitively small in view of proposals by Garg et al. (2025) to explain the lower limits of void magnetization by the superposition of dipoles from the far-field of galaxies.

We thank the referee for a constructive review. We acknowledge stimulating discussions with Ruth Durrer, Deepen Garg, and Jennifer Schober. This research was supported in part by the Swedish Research Council (Vetenskapsrådet) under grant No. 2025-05957, the National Science Foundation under grants No. NSF AST-2307698, AST-2408411, and NASA Award 80NSSC22K0825. OG acknowledges support from a Wallenberg Academy Fellowship (PI Azadeh Fattahi). Additionally, OG is supported by the Swedish Research Council (Vetenskapsrådet) under contracts 2022-04283 and 2019-02337 and additionally by the Göran Gustafsson Foundation for Research in Natural Sciences and Medicine. AN is partially supported by the French National Research Agency (ANR) grant ANR-24-CE31-4686. FV has been partially supported by Fondazione Cariplo and Fondazione CDP, through grant n° Rif: 2022-2088 CUP J33C22004310003 for the “BREAK-THRU” project. We acknowledge the allocation of computing resources provided by the Swedish National Allocations Committee at the Center for Parallel Computers at the Royal Institute of Technology in Stockholm.

Software and Data Availability. The source code used for the simulations of this study, the PENCIL CODE (Pencil Code Collaboration et al. 2021), is freely available on <https://github.com/pencil-code>. The simulation setups and corresponding input and reduced output data are freely available on <http://doi.org/10.5281/zenodo.18564321>.

REFERENCES

- Aramburo-García, A., et al. 2021, *Mon. Not. R. Astron. Soc.*, 502, 6012, doi: [10.1093/mnras/stab391](https://doi.org/10.1093/mnras/stab391)
- . 2022, *Mon. Not. R. Astron. Soc.*, 514, 2656, doi: [10.1093/mnras/stac1460](https://doi.org/10.1093/mnras/stac1460)
- Armillotta, L., Ostriker, E. C., & Linzer, N. B. 2025, *ApJ*, 989, 140, doi: [10.3847/1538-4357/adea68](https://doi.org/10.3847/1538-4357/adea68)
- Beck, R. 1991, *A&A*, 251, 15
- Bonanno, A. 2016, *ApJL*, 833, L22, doi: [10.3847/2041-8213/833/2/L22](https://doi.org/10.3847/2041-8213/833/2/L22)
- Bonanno, A., & Del Sordo, F. 2017, *A&A*, 605, A33, doi: [10.1051/0004-6361/201731330](https://doi.org/10.1051/0004-6361/201731330)
- Bondarenko, K., Boyarsky, A., Korochkin, A., et al. 2022, *A&A*, 660, A80
- Brandenburg, A., Donner, K. J., Moss, D., et al. 1993, *A&A*, 271, 36
- Brandenburg, A., Haugen, N. E. L., & Babkovskaia, N. 2011, *PhRvE*, 83, 016304, doi: [10.1103/PhysRevE.83.016304](https://doi.org/10.1103/PhysRevE.83.016304)
- Brandenburg, A., Moss, D., & Tuominen, I. 1992, *A&A*, 265, 328
- Brandenburg, A., & Stepanov, R. 2014, *ApJ*, 786, 91, doi: [10.1088/0004-637X/786/2/91](https://doi.org/10.1088/0004-637X/786/2/91)
- Brandenburg, A., Tuominen, I., & Krause, F. 1990, *Geophys. Astrophys. Fluid Dynam.*, 50, 95, doi: [10.1080/03091929008219875](https://doi.org/10.1080/03091929008219875)
- Chandrasekhar, S., & Kendall, P. C. 1957, *ApJ*, 126, 457, doi: [10.1086/146413](https://doi.org/10.1086/146413)
- Chiu, H.-H. S., Ruszkowski, M., Thomas, T., Werhahn, M., & Pfrommer, C. 2024, *ApJ*, 976, 136, doi: [10.3847/1538-4357/ad84e9](https://doi.org/10.3847/1538-4357/ad84e9)
- Einstein, A. 1905, *Ann. Phys.*, 322, 549, doi: [10.1002/andp.19053220806](https://doi.org/10.1002/andp.19053220806)
- Elstner, D., Golla, G., Rüdiger, G., & Wielebinski, R. 1995, *A&A*, 297, 77

- Elstner, D., Meinel, R., & Rüdiger, G. 1990, *Geophys. Astrophys. Fluid Dynam.*, 50, 85, doi: [10.1080/03091929008219874](https://doi.org/10.1080/03091929008219874)
- Freidberg, J. P. 2014, *Ideal MHD*, doi: [10.1017/CBO9780511795046](https://doi.org/10.1017/CBO9780511795046)
- Garg, D., Durrer, R., & Schober, J. 2025, <https://arxiv.org/abs/2505.14774>
- Ghasemi-Nodehi, M., Tabatabaei, F. S., Sargent, M., et al. 2022, *MNRAS*, 515, 1158, doi: [10.1093/mnras/stac1393](https://doi.org/10.1093/mnras/stac1393)
- Ghosh, O., Brandenburg, A., Caprini, C., Neronov, A., & Vazza, F. 2026, *PhRvD*, 113, 023523, doi: [10.1103/4114-mgsp](https://doi.org/10.1103/4114-mgsp)
- Ginzburg, V. L., & Syrovatskii, S. I. 1965, *ARA&A*, 3, 297, doi: [10.1146/annurev.aa.03.090165.001501](https://doi.org/10.1146/annurev.aa.03.090165.001501)
- Ivanova, T. S., & Ruzmaikin, A. A. 1977, *SvA*, 21, 479
- Jabbari, S., Brandenburg, A., Kleorin, N., Mitra, D., & Rogachevskii, I. 2015, *ApJ*, 805, 166, doi: [10.1088/0004-637X/805/2/166](https://doi.org/10.1088/0004-637X/805/2/166)
- Jakab, P., & Brandenburg, A. 2021, *A&A*, 647, A18, doi: [10.1051/0004-6361/202038564](https://doi.org/10.1051/0004-6361/202038564)
- Kitchatinov, L. L., & Rüdiger, G. 1995, *A&A*, 299, 446
- Krause, F., & Rädler, K.-H. 1980, *Mean-Field Magnetohydrodynamics and Dynamo Theory* (Oxford: Pergamon Press)
- Meinel, R., Elstner, D., & Ruediger, G. 1990, *A&A*, 236, L33
- Moffatt, H. K. 1978, *Magnetic Field Generation in Electrically Conducting Fluids* (Cambridge: Cambridge University Press)
- Murray, J. D., Stanley, E. A., & Brown, D. L. 1986, *Proc. Roy. Soc. Lond. Ser. B*, 229, 111, doi: [10.1098/rspb.1986.0078](https://doi.org/10.1098/rspb.1986.0078)
- Oei, M. S. S. L. 2025, private information
- Parker, E. N. 1979, *Cosmical Magnetic Fields: Their Origin and Their Activity* (Oxford: Clarendon Press)
- Pencil Code Collaboration, Brandenburg, A., Johansen, A., et al. 2021, *J. Open Source Software*, 6, 2807, doi: [10.21105/joss.02807](https://doi.org/10.21105/joss.02807)
- Peron, G., Aharonian, F., Casanova, S., Yang, R., & Zanin, R. 2021, *ApJL*, 907, L11, doi: [10.3847/2041-8213/abcaa9](https://doi.org/10.3847/2041-8213/abcaa9)
- Perri, B., Brun, A. S., Strugarek, A., & Réville, V. 2021, *ApJ*, 910, 50, doi: [10.3847/1538-4357/abe2ac](https://doi.org/10.3847/1538-4357/abe2ac)
- Pfrommer, C., Werhahn, M., Pakmor, R., Girichidis, P., & Simpson, C. M. 2022, *MNRAS*, 515, 4229, doi: [10.1093/mnras/stac1808](https://doi.org/10.1093/mnras/stac1808)
- Priest, E. R. 1982, *Solar magnetohydrodynamics.*, Vol. 21 (Cambridge University Press)
- Rempel, M. 2006, *ApJ*, 647, 662, doi: [10.1086/505170](https://doi.org/10.1086/505170)
- Rybicki, G. B., & Lightman, A. P. 1986, *Radiative Processes in Astrophysics* (Wiley-VCH Verlag GmbH & Co. KGaA)
- Schüssler, M. 1979, *A&A*, 72, 348
- Seller, K., & Sigl, G. 2025, On the contribution of galaxies to the magnetic field in cosmic voids. <https://arxiv.org/abs/2510.08025>
- Steenbeck, M., & Krause, F. 1969, *Astron. Nachr.*, 291, 49, doi: [10.1002/asna.19692910201](https://doi.org/10.1002/asna.19692910201)
- Stix, M. 1975, *A&A*, 42, 85
- Taziaux, S., Müller, A., Adebahr, B., et al. 2025, *A&A*, 696, A226, doi: [10.1051/0004-6361/202453311](https://doi.org/10.1051/0004-6361/202453311)
- Vazza, F., Gheller, C., Zanetti, F., et al. 2025, *A&A*, 696, A58, doi: [10.1051/0004-6361/202451709](https://doi.org/10.1051/0004-6361/202451709)
- Werhahn, M., Pfrommer, C., Girichidis, P., Puchwein, E., & Pakmor, R. 2021, *MNRAS*, 505, 3273, doi: [10.1093/mnras/stab1324](https://doi.org/10.1093/mnras/stab1324)
- Yang, W. H., Sturrock, P. A., & Antiochos, S. K. 1986, *ApJ*, 309, 383, doi: [10.1086/164610](https://doi.org/10.1086/164610)

APPENDIX

A. DISPERSION RELATION FOR A DYNAMO WITH CONSTANT COEFFICIENTS

To illuminate the mean-field dynamo behavior for a finite speed of light and to provide a benchmark for testing purposes, we discuss here the case of an α^2 dynamo with constant coefficients. Seeking solutions proportional to $\exp(\gamma t + i\mathbf{k} \cdot \mathbf{x})$, the dispersion relation $\gamma(\mathbf{k})$ can be obtained by solving for the roots of

$$\left[\gamma + \eta_{\text{eff}} k^2 \left(1 + \frac{\gamma^2}{c^2 k^2} \right) \right]^2 - \alpha^2 k^2 = 0. \quad (\text{A1})$$

In the limit $c \rightarrow \infty$, the dispersion relation agrees with the conventional one,

$$\gamma = \pm |\alpha| k - \eta_{\text{eff}} k^2. \quad (\text{A2})$$

Figure 8 shows $\gamma(\alpha)$ for a fixed value of $k = k_1$ and three values of $c/\eta_{\text{eff}} k_1$. The dependence matches the conventional one for $c \rightarrow \infty$. We see that the effect of a finite speed of light is to lower the value of γ .

For $\alpha = 0$, the growth rate is always negative. There are then two branches given by

$$\gamma_{\pm} = - \left[1 \pm \sqrt{1 - (2\eta_{\text{eff}} k/c)^2} \right] c^2 / 2\eta_{\text{eff}}. \quad (\text{A3})$$

For $k > c/2\eta_{\text{eff}}$, i.e., for $k/k_1 > c/2\eta_{\text{eff}} k_1$, γ is complex, i.e., the solutions are oscillatory with the growth rate $\text{Re}\gamma = -c^2/2\eta_{\text{eff}}$, which is independent of k . This

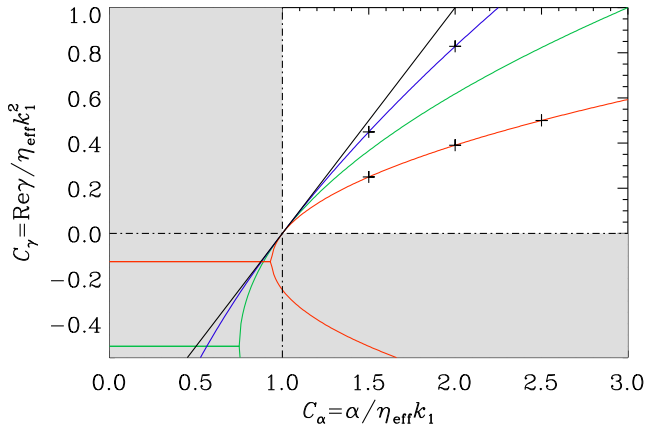


Figure 8. Growth rate versus dynamo number $\alpha/\eta_{\text{eff}} k_1$ for a fixed value of $k = k_1$ and $c/\eta_{\text{eff}} k = 0.5$ (red), 1 (green), and 2 (blue). The gray areas mark the regions of no growth. The conventional dependence for $c \rightarrow \infty$ corresponds to the black line. The black plus signs refer to data points obtained with the PENCIL CODE.

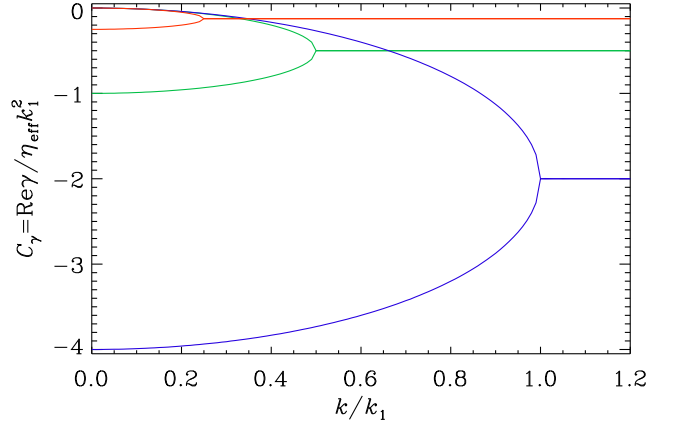


Figure 9. Normalized growth rate versus k/k_1 for $\alpha = 0$ and $c/\eta_{\text{eff}} k_1 = 0.5$ (red), 1 (green), and 2 (blue). For $k > c/2\eta_{\text{eff}}$, the two solutions are oscillatory with a complex conjugated pair of eigenvalues, whose real part is independent of k .

is shown in Figure 9, where we plot the negative normalized growth rate versus k/k_1 for different values of $c/\eta_{\text{eff}} k_1$. Evidently, only for $c/\eta_{\text{eff}} k_1 > 2$ the solutions are nonoscillatory for all wavenumbers.

For an exponentially growing magnetic field, the spatial spreading can be described by writing $\overline{\mathbf{B}} \propto e^{-\kappa(z - c_{\text{front}} t)}$, where c_{front} is the front speed, $\kappa c_{\text{front}} = \gamma$ is the growth rate, and $\kappa = k$. This relation is only valid outside the dynamo-active region, where $\alpha = 0$. Since the effect of a finite speed of light is to lower the value of γ , this also lowers the front speed γ/k . For the conventional dispersion relation, the front speed is

$$c_{\text{front}} = \gamma/k = |\alpha| - \eta_{\text{eff}} k. \quad (\text{A4})$$

For finite values of c , the front speed is lowered, except for the marginal point when k exceeds the critical value below which dynamo action is possible. This is shown in Figure 10 for three finite values of $c/\eta_{\text{eff}} k$. We see that the line for $c/\eta_{\text{eff}} k = 2$ is already rather close to the case $c \rightarrow \infty$. As discussed in the bulk of the present paper, $c/\eta_{\text{eff}} k$ is indeed very large for realistic values of η_{eff} and k . Therefore, the Faraday displacement current can indeed be neglected for all practical purposes.

As expected, the front speed never exceeds the speed of light. By contrast, however, the input parameters α and $\eta_{\text{eff}} k$, which also have the dimension of a speed, can exceed the value of c . Whether or not this can physically be realized is questionable.

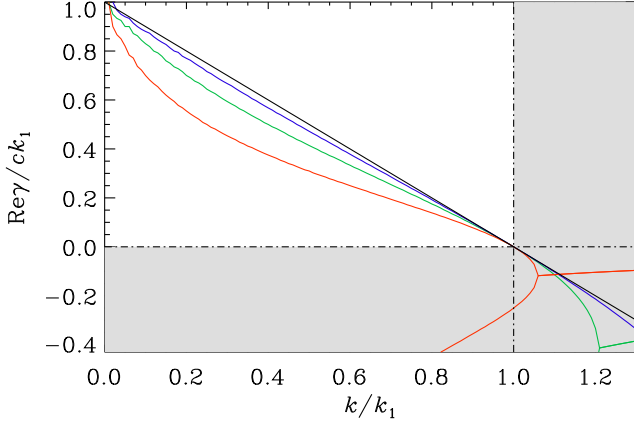


Figure 10. Front speed γ/k (in units of c) versus k (in units of c/η_{eff}) for $\alpha/c = 1$ and $c/\eta_{\text{eff}}k = 0.5$ (red), 1 (green), and 2 (blue). As in Figure 8, the gray areas mark the regions of no growth. The conventional line for $c \rightarrow \infty$ corresponds to the black line.

B. POWER LAW GROWTH OF η_{eff}

For the quadrupolar case, the inversely quadratic radial fall-off is still approximately obeyed even when η_{eff} is not constant for $r > R$. This is demonstrated Figure 11, where we compare the mean radial magnetic field profiles for Runs G, G', and G''. The slopes do not depart markedly from the r^{-2} decay. For a more quantitative demonstration, we show for Runs G' and G'' also the profiles compensated by r^{+n} with $n = 2.16$ and with $n = 2.23$, respectively. This confirms that the decay exponents given in Table 1 are accurately determined.

C. DERIVATION OF EQUATION (41)

The purpose of this appendix is to provide the detailed derivation of Equation (42). Following Rybicki & Lightman (1986), for a powerlaw distribution of CRs such as $N(E)dE = CE^{-\zeta}dE$, $E_{\text{min}} < E < E_{\text{max}}$ with a particle distribution index ζ corresponding to the spectral index s as $s = (\zeta - 1)/2$ such that $P_{\text{tot}}(\omega) \propto \omega^{-(\zeta-1)/2}$, normalization can be determined from the cosmic ray number density

$$n_{\text{CR}} = C \frac{E_{\text{max}}^{1-\zeta} - E_{\text{min}}^{1-\zeta}}{1 - \zeta}, \quad (\text{C5})$$

for $E_{\text{min}} < E < E_{\text{max}}$ known as the band-limited case. However, if $E_{\text{max}} \rightarrow \infty$, normalization C depends only on the threshold energy E_{min} for $\zeta > 1$ as

$$C = n_{\text{CR}}(\zeta - 1)E_{\text{min}}^{\zeta-1}. \quad (\text{C6})$$

The total synchrotron power per unit volume per unit frequency irradiated by such a population of CR can be

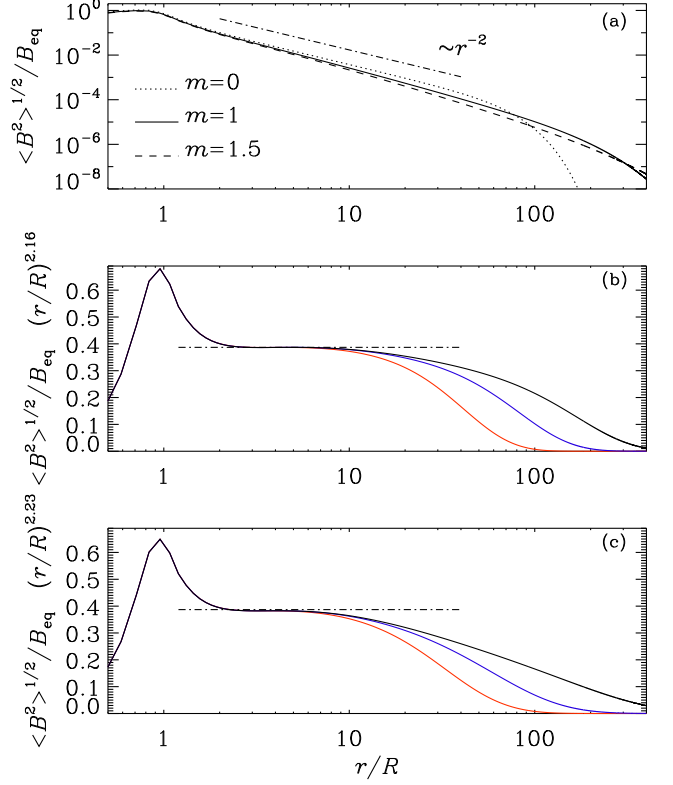


Figure 11. (a) Radial magnetic field profiles for the quadrupolar Runs G, G', and G''. Runs G' and G'' have a radially increasing $\eta_{\text{eff}}(r)$ profile. In panels (b) and (c), the mean magnetic field profiles are compensated by $r^{2.16}$ and $r^{2.23}$, respectively. The red, blue, and black lines refer to the times $t/\tau_{\text{diff}} = 100, 250,$ and 600 for Run G', and $t/\tau_{\text{diff}} = 50, 100,$ and 250 for Run G''.

written as

$$P_{\text{tot}}(\nu) = \frac{\sqrt{3}q^3CB\sin\alpha}{mc^2(\zeta+1)}C_2\left(\frac{2\pi m c\nu}{3qB\sin\alpha}\right)^{\frac{1-\zeta}{2}}, \quad (\text{C7})$$

Based on this, the optically thick surface brightness can be expressed in general as

$$I_\nu \propto n_{\text{CR}}(> E_{\text{min}})E_{\text{min}}^{\zeta-1}B^{(1+\zeta)/2}L\nu^{(1-\zeta)/2}. \quad (\text{C8})$$

Taking equipartition value of the magnetic field $B = B_{\text{eq}}$, averaging over the pitch angle factor $\langle \sin^{(1+\zeta)/2}\alpha \rangle$, and finally setting the index $\zeta = 3$, we obtain an optically thick surface brightness of the form

$$I_\nu \approx 5 \times 10^{-6} \text{ Jy/sr} \left(\frac{n_{\text{CR}}}{10^{-7} \text{ cm}^{-3}}\right) \left(\frac{E_{\text{min}}}{100 \text{ MeV}}\right)^2 \times \left(\frac{B}{1 \mu\text{G}}\right)^2 \left(\frac{L}{1 \text{ kpc}}\right) \left(\frac{\nu}{150 \text{ MHz}}\right)^{-1}. \quad (\text{C9})$$

Replacing $(\nu/150 \text{ MHz})^{-1}$ by $(\lambda/2 \text{ m})$ and using $E_{\text{min}} = 100 \text{ MeV}$, we arrive at Equation (42).